**ADVANCED
MATERIALS
INTERFACES**

Supporting Information

High-Performance Transparent Broadband Microwave
Absorbers

*Heyan Wang, Yilei Zhang, Chengang Ji, Cheng Zhang,
Zhengang Lu,* Yunfei Liu, Zhibo Cao, Jing Yuan, Jiubin
Tan, and L. Jay Guo**

Supporting Information

High-performance Transparent Broadband Microwave Absorbers

Heyan Wang, Yilei Zhang, Chengang Ji, Cheng Zhang, Zhengang Lu*, Yunfei Liu, Zhibo Cao, Jing Yuan, Jiubin Tan and L. Jay Guo

Dr. H. Wang, Y. Zhang, Y. Liu, Z. Cao, J. Yuan, Prof. Z. Lu, Prof. J. Tan
Ultra-precision Optical & Electronic Instrument Engineering Center, Harbin Institute of Technology, Harbin 150001, China
Key Lab of Ultra-precision Intelligent Instrumentation (Harbin Institute of Technology), Ministry of Industry and Information Technology, Harbin 150080, China
Dr. C. Ji, Prof. L. Jay Guo
Department of Electrical Engineering and Computer Science, University of Michigan, Ann Arbor, MI 48109, USA
Prof. C. Zhang,
School of Optical and Electronic Information & Wuhan National Laboratory for Optoelectronics, Huazhong University of Science and Technology, China.

E-mail: luzhengang@hit.edu.cn; guo@umich.edu

Section 1.1: Transfer matrix method (TMM)

As shown in Figure S1, the complex refractive index and thickness of the *jth* layer are $\tilde{n}_j = n_j + ik_j$

and d_j, respectively. Subsequently, we can obtain the interface matrix I_{jk} and phase matrix L_j of

each layer based on the Fresnel formulas. The S transmission matrix of the multilayered structure

can be calculated using Equation 6. Finally, we can obtain the microwave transmission $T = t^2$,

microwave reflection $R = r^2$, and the absorption $A = 1 - R - T$ of the multilayered structure through

the TMM. For the MGSS structure, graphene, silica, and ultrathin Ag films can be assigned to the

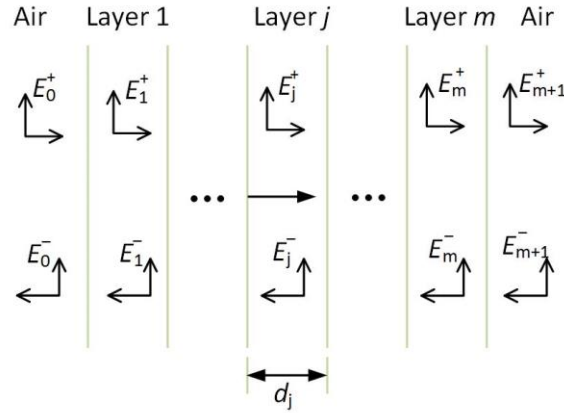corresponding layers in Figure S1.

Figure S1. A general multilayered structure having *m* layers.

$$I_{jk} = \frac{1}{t_{jk}} \begin{bmatrix} 1 & r_{jk} \\ r_{jk} & 1 \end{bmatrix} \tag{1}$$

$$r_{jk} = \frac{\tilde{n}_j - \tilde{n}_k}{\tilde{n}_j + \tilde{n}_k} \tag{2}$$

$$t_{jk} = \frac{2\tilde{n}_j}{\tilde{n}_j + \tilde{n}_k} \tag{3}$$

$$L_j = \begin{bmatrix} e^{-i\frac{2\pi}{\lambda}\tilde{n}_j d_j} & 0 \\ 0 & e^{i\frac{2\pi}{\lambda}\tilde{n}_j d_j} \end{bmatrix} \tag{4}$$

$$\begin{bmatrix} E_0^+ \\ E_0^- \end{bmatrix} = S \begin{bmatrix} E_{m+1}^+ \\ E_{m+1}^- \end{bmatrix} \tag{5}$$

$$S = \begin{bmatrix} S_{11} & S_{12} \\ S_{21} & S_{22} \end{bmatrix} = \left(\prod_{v=1}^{m} I_{(v-1)v} L_v \right) \cdot I_{m(m+1)} \tag{6}$$

$$r = \frac{E_0^-}{E_0^+} = \frac{S_{21}}{S_{11}} \tag{7}$$

$$t = \frac{E_{m+1}^+}{E_0^+} = \frac{1}{S_{11}} \tag{8}$$

Section 1.2: Electric field intensity calculation

Based on the TMM and established transmission model, as shown in Figure S1, the electric field intensity $E_j(x)$ and energy absorption rate $Q(x)$ at different positions can be calculated using Equations (9)–(22) as follows:

$$S = S_j' L_j S_j'' \tag{9}$$

$$\begin{bmatrix} E_0^+ \\ E_0^- \end{bmatrix} = S_j' \begin{bmatrix} E_j'^+ \\ E_j'^- \end{bmatrix} \tag{10}$$

$$S_j' = \begin{bmatrix} S_{j11}' & S_{j12}' \\ S_{j21}' & S_{j22}' \end{bmatrix} = \left(\prod_{v=1}^{j-1} I_{v(v-1)} L_v \right) \cdot I_{(j-1)j} \tag{11}$$

$$\begin{bmatrix} E_j''^+ \\ E_j''^- \end{bmatrix} = S_j'' \begin{bmatrix} E_{m+1}^+ \\ E_{m+1}^- \end{bmatrix} \tag{12}$$

$$S_j'' = \begin{bmatrix} S_{j11}'' & S_{j12}'' \\ S_{j21}'' & S_{j22}'' \end{bmatrix} = \left(\prod_{v=j+1}^{m} I_{v(v-1)} L_v \right) \cdot I_{m(m+1)} \tag{13}$$

$$r_j' = \frac{S_{j21}'}{S_{j11}'}, t_j' = \frac{1}{S_{j11}'} \tag{14}$$

$$r_j'' = \frac{S_{j21}''}{S_{j11}''}, t_j'' = \frac{1}{S_{j11}''} \tag{15}$$

$$t_j^+ = \frac{E_j^+}{E_0^+} = \frac{t_j'}{1 - r_j' r_{j-}'' \cdot e^{i2\xi_j d_j}} \tag{16}$$

$$t_j^- = \frac{E_j^-}{E_0^+} \frac{t_j' r_j'' \cdot e^{i2\xi_j d_j}}{1 - r_j' r_{j-}'' \cdot e^{i2\xi_j d_j}} = t_j^+ r_j'' \cdot e^{i2\xi_j d_j} \tag{17}$$

$$E_j(x) = E_j^+(x) + E_j^-(x) = \left[t_j^+ e^{i\xi_j x} + t_j^- e^{-i\xi_j x} \right] E_0^+ \tag{18}$$

$$E_j(x) = \frac{S_{j11}^{"} \cdot e^{-i\xi_j(d_j-x)} + S_{j21}^{"} \cdot e^{i\xi_j(d_j-x)}}{S_{j11}^{'}S_{j11}^{"} \cdot e^{-i\xi_j d_j} + S_{j12}^{'}S_{j21}^{"} \cdot e^{i\xi_j d_j}} E_0^+ \tag{19}$$

$$\xi_j = \frac{2\pi}{\lambda}\tilde{n}_j \tag{20}$$

$$Q(x) = \frac{1}{2}c\varepsilon_0\alpha_j n_j \left|E_j(x)\right|^2 \tag{21}$$

$$\alpha_j = \frac{4\pi\kappa_j}{\lambda} \tag{22}$$
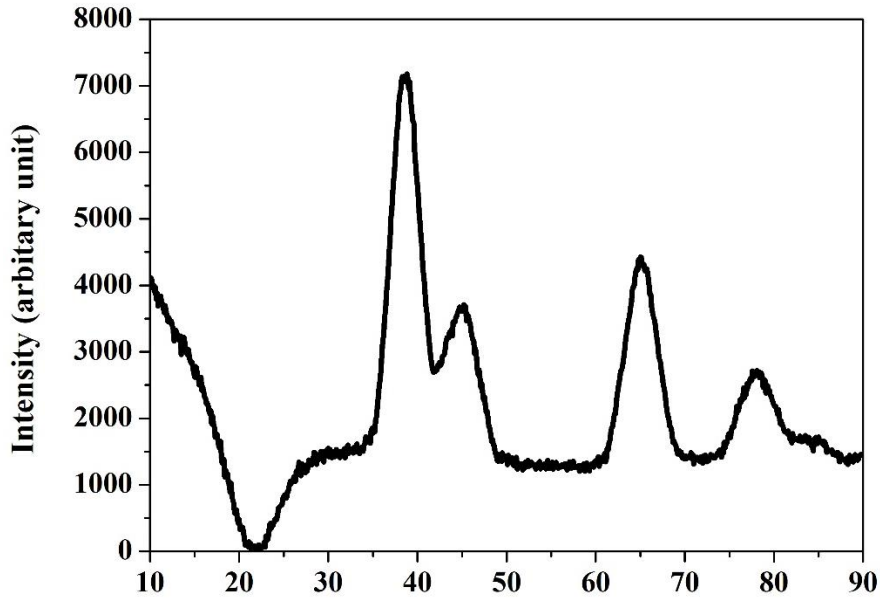
2. XRD result of doped Ag film

Figure S2. As can be seen from the figure that all diffraction peaks can be assigned to the cubic Ag. Since doping element's concentration is low, the doped Ag film still maintains the structural properties of pure Ag.
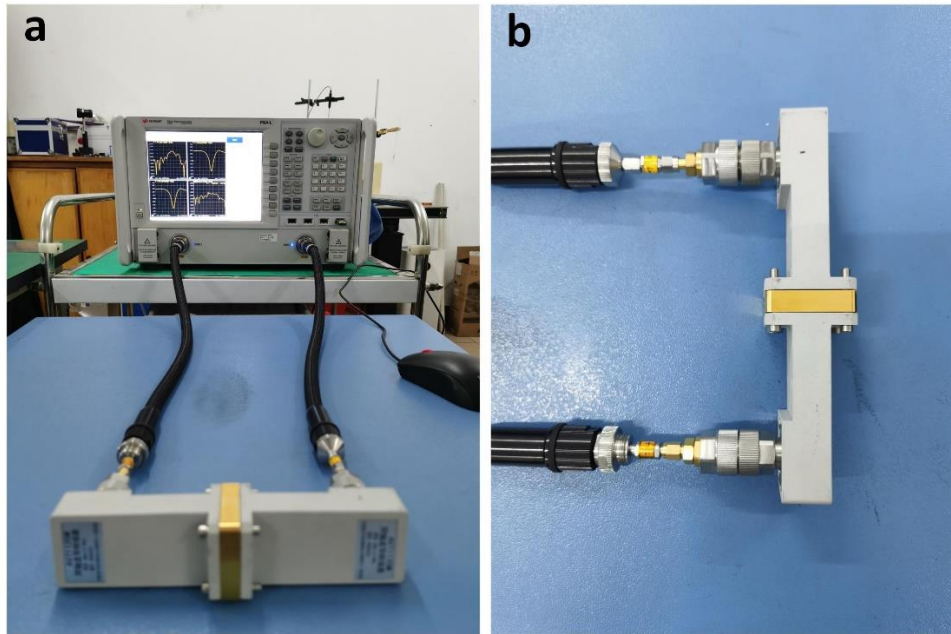
3. Microwave measurement setup

Figure S3. a) Microwave measurement setup composed of vector network analyzer (KEYSIGHT N5234A), waveguide-to-coaxial adapter, and waveguide. b) A standard rectangular waveguide in the Ku band. It should be noted that four different waveguides with different sizes were used to measure microwave absorption performance in the X, Ku, K, and Ka bands, and the MGSS samples were cut into the appropriate sizes and inserted into the waveguides.

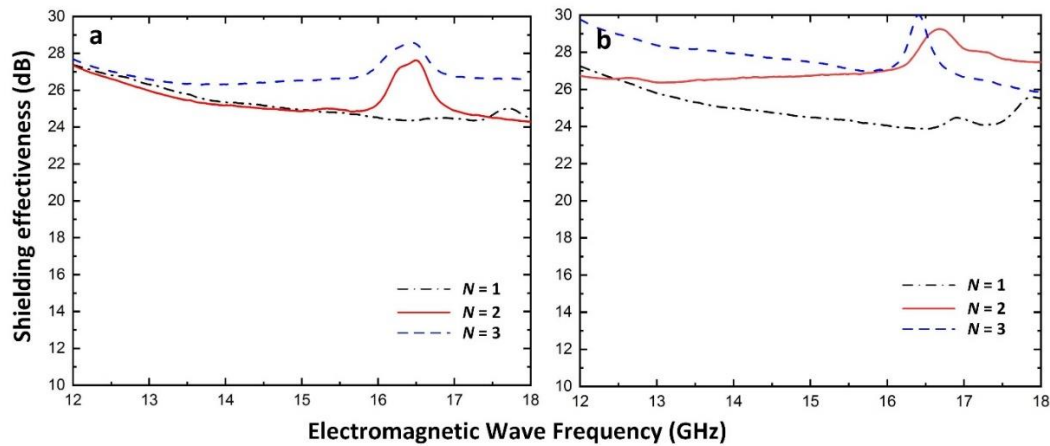4. **Measured shielding effectiveness of MGSS samples in the Ku band**

Figure S4. Measured shielding effectiveness of the MGSS in the Ku band. a) $d = 1$ mm. b) $d = 2$ mm. It should be noted that the measured shielding effectiveness in different bands is nearly the same, and MGSS samples at different silica thickness show the similar shielding capability of approximately 27 dB. The shielding effectiveness of the MGSS with more graphene/silica units is slightly higher than the MGSS with $N = 1$.

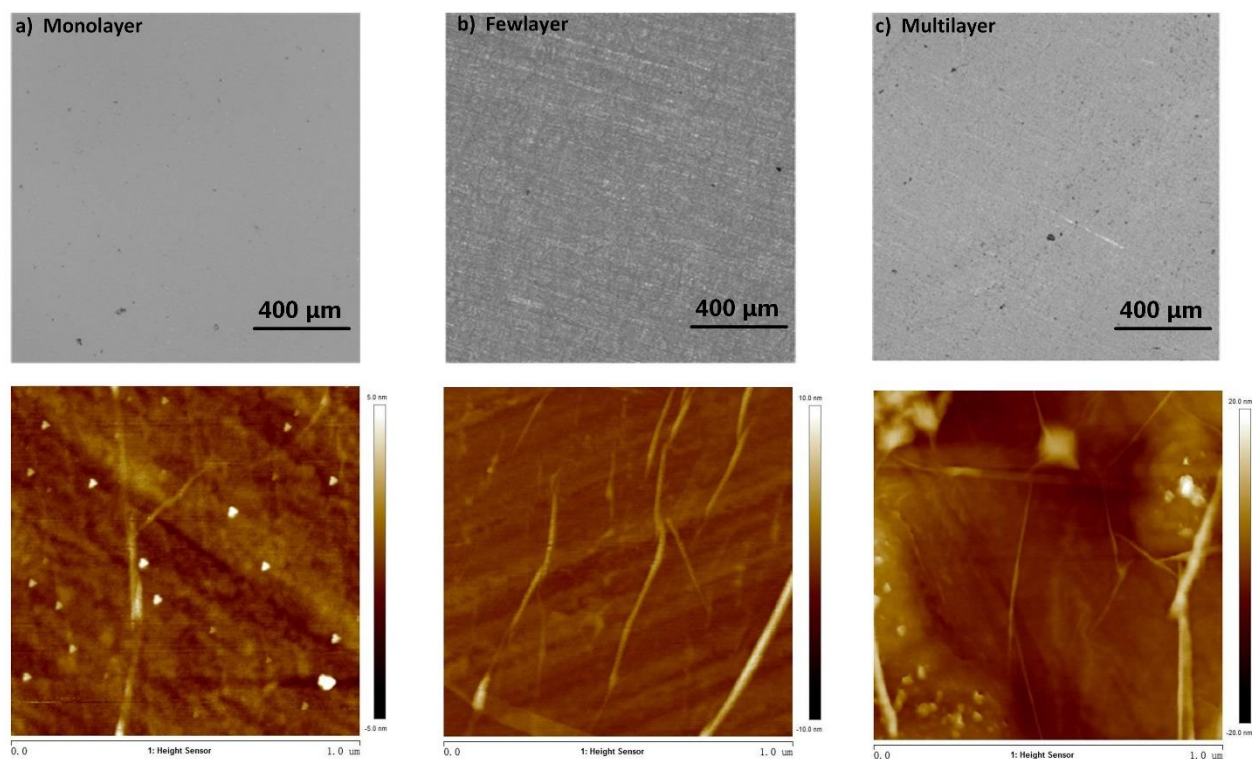5. **Surface morphology of CVD-grown graphene films**

Figure S5. We characterized the transferred graphene using confocal microscope and atomic force microscope (AFM), and it is clear that there are some wrinkles on the sample without too much defects, further verifying high-quality of the prepared graphene. In addition, white dots on the surface in AFM images are graphene/polymethyl methacrylate (PMMA) residuals after removing process.

6. Cavity absorption performance at different Fermi levels of graphene
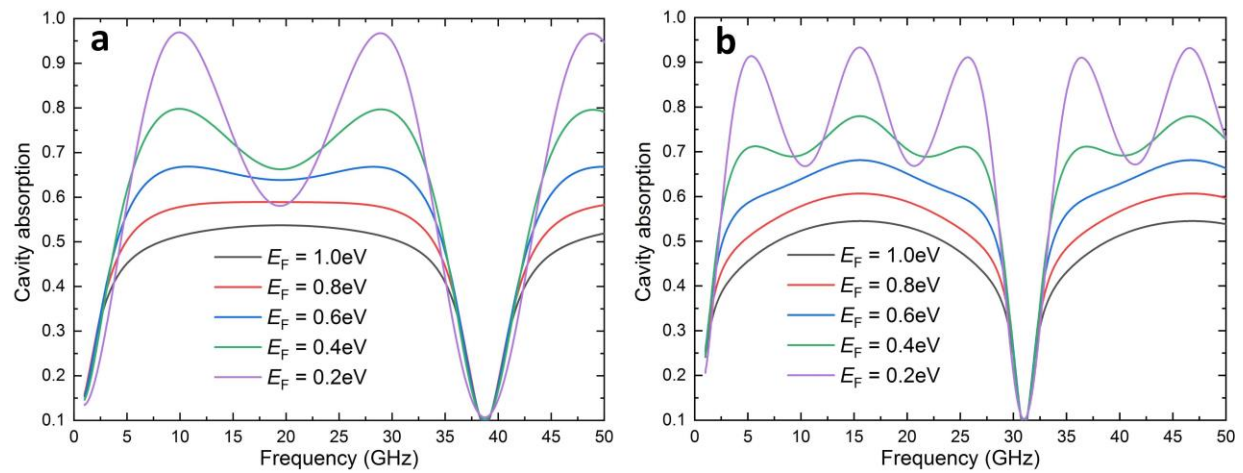

Figure S6. Calculated cavity absorption of the MGSS at different Fermi energy levels of graphene.

a) $N = 2$, $d = 2$ mm, b) $N = 3$, $d = 2.5$ mm. It is clear that peak absorption varied significantly by

changing the Fermi energy levels of graphene, which resulted from the changed coupling states at

resonances based on coupled mode theory.

7. Photographs of fabricated MGSS cavities with different layers of graphene
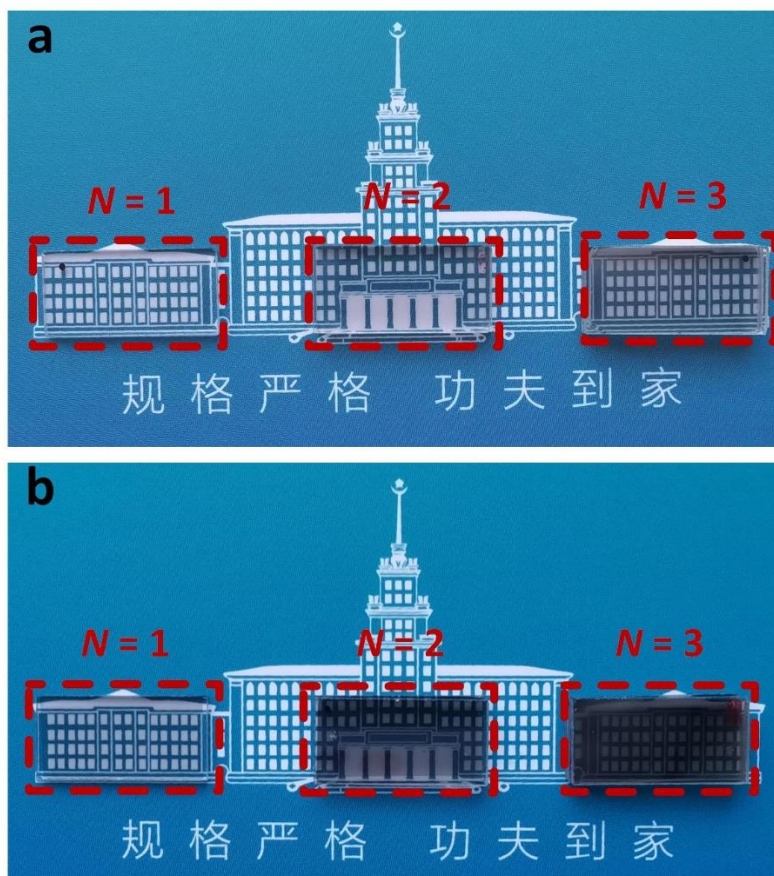
Figure S7. Photographs of the fabricated MGSS (d = 1mm) composed of a) few-layer graphene and b) multi-layer graphene. It is clear that the transparency of samples is decreasing with an increase in the number of the graphene/silica stacks.

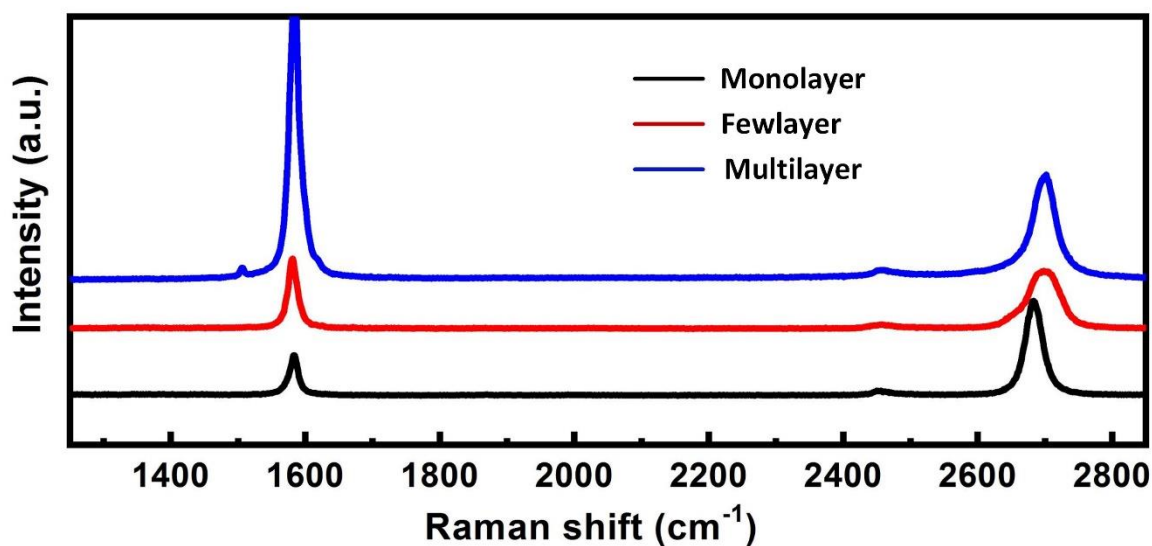8. **Raman spectra of CVD-grown graphene films**

Figure S8. We measured the Raman spectra of the chemical vapor deposition (CVD)-grown graphene at different layer numbers at the laser wavelength of 532 nm. All spectra exhibit the typical peak features of graphene, which include *G* and 2*D* bands, verifying the existence of the graphene. Furthermore, it is clear that the intensity ratio of *G* to 2*D* gradually increases with the increase in the number of graphene layers, further indicating the features of graphene at different layers as previous studies reported.